Chaos, Solitons and Fractals 207 (2026) 117979

Contents lists available at ScienceDirect

Chaos, Solitons and Fractals

journal homepage: www.elsevier.com/locate/chaos

Parameter-driven stabilization of gradient-induced asymmetric solitons in $\mathcal{PT}$-symmetric media: Comprehensive mapping of potential effects in 2D nonlinear waveguides

Jaseera C.P. [a,b,*], Aysha Muhsina K. [a]

[a] Department of Physics, Government Arts and Science College, Kozhikode, 673018, Kerala, India
[b] Department of Physics, Government College, Madappally, 673102, Kerala, India

ARTICLE INFO

Keywords:
Nonlinear system
Higher-order effects
Space modulated nonlinearity
Gradient-induced asymmetry
Collision dynamics
$\mathcal{PT}$-symmetric potential
Stability analysis

ABSTRACT

We investigate the propagation and stabilization of gradient-induced asymmetric solitons in a two-dimensional Modified Nonlinear Schrodinger (MNLS) framework with spatially varying nonlinearity. In the absence of external modulation, the asymmetry generates a transverse nonlinear momentum that drives the beam away from the center, producing both amplitude change and systematic drift. We show that a parity–time ($\mathcal{PT}$) symmetric imaginary potential, introduced as a transverse gain—loss landscape, provides an effective mechanism to counteract this gradient-induced asymmetry. By modulating the parameter space of the steepening strength, imaginary-potential coefficient, real-potential depth, nonlinearity and diffraction parameter we identify unique points at which the nonlinear flux, diffraction, and $\mathcal{PT}$–induced transverse energy exchange reach a well-defined balance condition. At these operating space, the soliton recovers a stable propagation state with suppressed drift, preserved beam width, and nearly constant amplitude. When the $\mathcal{PT}$–symmetric potential strength is below or above this balancing value, the beam exhibits characteristic signatures such as spreading-dominated decay, oscillatory focusing–de focusing cycles, or residual amplification, depending on the relative dominance of system parameters. In addition, we demonstrate collision dynamics, a propagation-based perturbation study that directly reveals the dynamical stability of these beams, complementing and validating the parameter-controlled stability analysis. The results establish a comprehensive picture of how $\mathcal{PT}$–symmetric gain–loss mechanisms can restore symmetry and stability in self-steepening optical solitons, and they provide guidelines for controlling nonlinear beam transport in engineered wave guiding structures with spatially modulated refractive index and nonlinearity.

1. Introduction

The conventional paradigm for combating optical beam spreading relies on confinement through waveguides or fibers, which impose physical boundaries to suppress diffraction. A more profound solution, however, emerges within the beam itself through the modification of the refractive index. Here, the medium's refractive index becomes a dynamic function of the light's intensity. This enables a remarkable phenomenon which is known as nonlinear self-focusing, which can enter into an equilibrium with diffraction, culminating in the formation of optical solitons [1–3]. These self-trapped wave packets are eigenstates of the nonlinear wave

* Corresponding author at: Department of Physics, Government Arts and Science College, Kozhikode, 673018, Kerala, India.
E-mail address: jaseerachilappurath@gmail.com (J. C.P.).

https://doi.org/10.1016/j.chaos.2026.117979
Received 12 December 2025; Received in revised form 18 January 2026; Accepted 21 January 2026
Available online 3 February 2026

equation, propagating without distortion, and representing a perfect intrinsic symmetry between wave spreading and self-induced focusing. This property, that has been extensively analyzed in the context of integrable and nearly integrable nonlinear systems, are studied in [4,5]. These phenomena generally arise under conditions of high optical intensity, such as during focused laser excitation. Because of their remarkable stability, solitons have been widely recognized as promising information carriers in advanced optical communication systems. They underpin key applications including high-speed data transmission, optical logic operations [6,7], ultrafast signal processing, pulse compression and splitting in nonlinear optics [8], as well as optical switching technologies [9,10].

The nonlinear Schrödinger equation (NLSE), given as

$$i\frac{\partial}{\partial z}\psi(x,z)+\zeta\frac{\partial^2}{\partial x^2}\psi(x,z)+n_2|\psi(x,z)|^2\psi(x,z)=0, \tag{1}$$

is a cornerstone framework for modeling the propagation of slowly varying wave envelopes in nonlinear optical media with diffraction effect enhanced by ζ. In the conventional (1+1)-dimensional media, the NLSE encapsulates the intricate balance between diffraction and nonlinear self-focusing effects. The nonlinear response arises through the intensity-dependent refractive index, expressed as $n(I)=n_0+n_2 I$, where n_0 represents the linear refractive index, n_2 denotes the Kerr coefficient, and $I=|\psi|^2$ corresponds to the local optical intensity. Recent studies of solitons have moved well beyond the classical cubic nonlinear Schrödinger (NLS) equation, incorporating higher-order mechanisms that govern their behavior in realistic optical systems. In practical photonic media, the simplifying assumptions of the standard NLS framework often fail, particularly in ultrashort-pulse and broadband regimes where higher-order dispersion and diffraction become crucial. Soliton stability in cubic-quintic fourth-order dispersive medium [11], optical solitons in a power law media with fourth-order dispersion [12], stability of one- and two-dimensional spatial solitons in higher order nonlinear system with fourth-order diffraction supported by $\mathcal{PT}$−symmetric potentials [13], formation of stable solitons in two-dimensional dissipative medium with constant loss [14,15] etc., establishes that these effects can induce asymmetric spectral broadening, pulse distortion, or even altered propagation stability [16].

Formation and stabilization of multi-hump solitons in saturable nonlinear medium [17], symmetry breaking of beams in the $\mathcal{PT}$−symmetric cubic–quintic competing saturable nonlinear medium [18], dynamical evolution of solitons in fractional Schrodinger equation with saturable nonlinearity [19,20], stability and excitation of nonlinear modes in spatially inhomogeneous nonlinear system [18,21], beam propagation in nonlocal nonlinear medium, where the refractive index at a given point is influenced by the surrounding field distribution [22–24], formation of two-dimensional spatial solitons in cubic–quintic–septimal nonlinear media with engineered gain–loss landscapes [13,25] etc are notable works in nonlinear medium with higher order effects.

Extending this direction, recent efforts have focused on spatially tailored nonlinear coefficients, where the nonlinear response varies across the medium [26–29]. Such engineered profiles — whether localized, graded, or structured — allow for the modification of soliton trajectories, thresholds, and interaction dynamics. Similarly, derivative nonlinear responses were originally formulated in the framework of temporal self-steepening, where the intensity-dependent modification of the group velocity results in waveform distortion and temporal asymmetry [30,31]. Pulse propagation dynamics, both in the normal and anomalous dispersive media, under self-steepening and self-frequency shifting [32,33], stable beam propagation by balanced dispersion and self-steepening mechanism [34], self-steepening of pulses in optical fibers [35], propagation of ultrashort optical pulses in quadratic-cubic nonlinear media with the self-steepening [36], etc. are dominating works in this field.

The idea of self-steepening has been generalized to spatial soliton models in order to capture nonlinear gradient-induced asymmetry and nonreciprocal propagation phenomena. These contributions, expressed as $\partial_x(|\psi|^2\psi)$, represent intensity-gradient-dependent corrections to the nonlinear response and thus provide a natural mechanism for describing asymmetric beam evolution, self-induced tilting, and directed energy transport [37]. Physically, they imply that the beam center propagates with a lower effective velocity compared to its wings, leading to the steepening of the intensity profile toward the trailing edge [38]. As a result, the beam envelope acquires an intrinsic asymmetry during propagation, and localized "shock-like" features may emerge at the rear boundary of the profile.

Motivated by these earlier studies, recent works have considered the incorporation of periodic $\mathcal{PT}$−symmetric potentials into the MNLS framework, which has been shown to mitigate both amplitude change and lateral displacement in self-steepening solitons [37]. Control of self-steepening effects on dissipative light bullets via linear potential has been discussed in [39]. Numerical investigation of the stability and bifurcation structure of solitary waves in a cubic-quintic system with self-steepening effect, along with external potentials has been discussed in [40]. Taken together, these extensions of the classical model — often referred to as MNLS equations — provide the theoretical framework for contemporary soliton engineering. By incorporating additional physical effects, they introduce new parameters for tailoring light localization and controlling nonlinear wave dynamics in complex media.

A major conceptual breakthrough in this direction arose from the seminal contributions of Bender and Boettcher [41,42], who demonstrated that a class of non-Hermitian Hamiltonians endowed with $\mathcal{PT}$-symmetry can sustain entirely real eigenvalue spectra. Subsequent studies confirmed that this property is realized when the refractive index profile varies spatially satisfying the $\mathcal{PT}$−symmetry conditions: the real component of the refractive index remains an even function of position, while the imaginary component — interpreted as spatially balanced gain and loss — is odd [43–46]. In such systems, the refractive index is expressed as $n(x)=n_R(x)+in_I(x)$, with $n_R(x)$ and $n_I(x)$ satisfies these symmetry requirements. Optical implementations of $\mathcal{PT}$−symmetry not only reproduce the fundamental quantum-inspired concepts introduced by Bender and Boettcher but also open pathways to novel beam transport, soliton formation, and stability mechanisms that arise uniquely from the interplay between nonlinearity, spatial tailoring, and balanced gain–loss landscapes.

Th existence and stability under the influence of fractional order effects with $\mathcal{PT}-$ symmetric potential [47], stable symmetric and antisymmetric dipole solitons and quadrupole solitons in the continuously-periodic photon moiré lattice [48], stability of

nonlinear beam in optical system supported by Scarff II potential [49], beam dynamics in 1D and 2D $\mathcal{PT}$−symmetric sinusoidal systems [50], $\mathcal{PT}$−symmetric coupled modes in transverse periodic and aperiodic potentials [51], dark soliton formation in $\mathcal{PT}$−symmetric system [52,53], localized eigenmodes in $\mathcal{PT}$−symmetric lattices [54], eigenmodes in cubic-quintic nonlinear media with $\mathcal{PT}$−symmetric hyperbolic potential [55], cubic-quintic eigenmodes in media supported by quartic harmonic potential [56], beam dynamics in $\mathcal{PT}$−symmetric coupler [57], dynamics of light bullets in inhomogeneous higher order nonlinear media with $\mathcal{PT}$−symmetric potentials [58], etc. are some notable works in this field.

In this study, we investigate the influence of an asymmetric nonlinear term — closely related to the self-steepening effect in ultrafast optics — on the propagation of two-dimensional spatial solitons which propagate along one direction and are confined in other two transverse coordinates. The presence of additional transverse degrees of freedom, which cause localized beams to be intrinsically more fragile and susceptible to collapse or diffraction, as widely reported [59–61]. Since it is marginally stable or unstable, its controlled propagation is a longstanding challenge. In this context, the self-steepening that breaks spatial symmetry and induces pronounced beam drift is significant. While self-steepening effects have been extensively studied earlier in the temporal domain and, to a limited extent, in one-dimensional spatial settings [37,38,40], their impact on two-dimensional beam stability remains largely unexplored. The present work goes beyond existing studies by demonstrating that, in a fully two-dimensional system, self-steepening leads to the simultaneous emergence of transverse drift and amplitude distortion, which cannot be mitigated by diffraction or nonlinearity alone.

To counteract these destabilizing effect, we introduce an engineered $\mathcal{PT}$−symmetric modification of the complex refractive index. In the two-dimensional domain, the interplay between spatially modulated nonlinearity and the $\mathcal{PT}$−symmetric gain–loss distribution creates a unique stabilization mechanism, where both amplitude oscillations and transverse displacements are markedly suppressed. These findings shed light on the design of robust 2D soliton states and demonstrate how $\mathcal{PT}$−symmetric engineering can be harnessed to regulate asymmetric beam dynamics in nonlinear optical media.

2. Theoretical model and nonlinear beam evolution

The beam dynamics in a system with spatially varying cubic nonlinearity, and an additional asymmetric contribution, can be modeled by the MNLS equation, which has the form

$$i\frac{\partial}{\partial z}\psi(x,y,z)+\zeta\nabla_{\perp}^{2}\psi(x,y,z)+\beta_{1}(x,y)|\psi(x,y,z)|^{2}\psi(x,y,z)+is\left(\frac{\partial}{\partial x}+\frac{\partial}{\partial y}\right)(|\psi(x,y,z)|^{2}\psi(x,y,z))=0. \tag{2}$$

Eq. (2) is a two-dimensional extension of NLSE [37,38,40]. Here, the operator $(\partial_x+\partial_y)$ accounts for nonlinear gradient effects along both transverse directions, allowing the model to capture multidimensional intensity-driven energy flow and beam deformation phenomena. The cubic nonlinearity (Kerr) with spatial inhomogeneity is represented by a position-dependent coefficient. $\beta_1(x,y)=G_3e^{\frac{-b^2(x^2+y^2)}{2}}$, where the parameter b controls the degree of spatial confinement of the nonlinear response [27]. This Gaussian profile establishes a nonlinear landscape such that larger values of b correspond to a more localized and sharply peaked nonlinearity at $x=0$, whereas smaller values of b lead to a broader distribution of the nonlinear effect.

The modulation of the nonlinear coefficient is interpreted as an effective spatially varying nonlinearity arising from controlled dopant distributions, thermal gradients, or structural modifications in the fiber core. In modern photonic systems, such tailoring can be realized through graded-index profiles, photonic crystal fiber designs, or femtosecond-laser-written waveguides, where both the linear and nonlinear refractive indices can be engineered simultaneously. Although earlier studies have demonstrated spatially localized nonlinear responses in colloidal or polymer-based planar waveguides [62,63], the same concept extends naturally to guided fiber systems. Here, the spatial dependence of $\beta_1(x,y)$ provides an additional degree of control over beam confinement, diffraction management, and nonlinear localization, enabling stable beam propagation under tailored refractive-index and gain–loss landscapes.

The optical field, $\psi(x,y,z)$ denotes the complex envelope of the electric field associated with a spatial optical beam. The parameter s represents the gradient-induced asymmetry and functions as a phenomenological measure of non-conservative effects or engineered flux imbalance that may arise in structured photonic systems with spatial non-uniformities [38]. Such asymmetry can be introduced through transverse modulation of nonlinear coefficients—practically achievable via thermal gradients or asymmetric doping in materials such as chalcogenide glasses and polymer waveguides. Within this framework, the parameter s acts as a tunable control variable that determines the strength of the induced asymmetry, thereby enabling the modeling of a wide range of physically plausible beam dynamics.

The beam propagation is investigated numerically using the finite difference method [64] and Fig. 1(a) illustrates the beam intensity profile $|\psi|^2$, obtained as the solution of Eq. (2) for the parameter set $\zeta=1$, $b=1.5$, $G_3=0.06$, and $s=0$. In the absence of the asymmetry term, the governing model reduces to the standard two-dimensional NLSE. The beam propagation exhibits complete transverse symmetry, with the input Gaussian, having the form $\psi(x,y,z)=Ae^{\frac{-(x^2+y^2)}{2a(z)^2}}$, where $a(z)$ stands for the width of beam, remaining centered throughout the evolution. The interplay between diffraction and spatially varying cubic self-focusing effect results in a stationary beam whose width, amplitude, and power remain nearly constant along the propagation direction. It is well known that the $2D$ cubic NLSE with uniform Kerr nonlinearity supports unstable bright solitons due to critical collapse [59–61]. In the present model, the spatial modulation of the cubic nonlinearity coefficient provides effective nonlinear confinement, suppressing collapse and allowing robust propagation over the distances considered, as illustrated in Fig. 1(a). This establishes the benchmark scenario for the system, serving as a baseline against which the impact of nonlinear gradient and $\mathcal{PT}$−symmetric effects can be systematically examined.

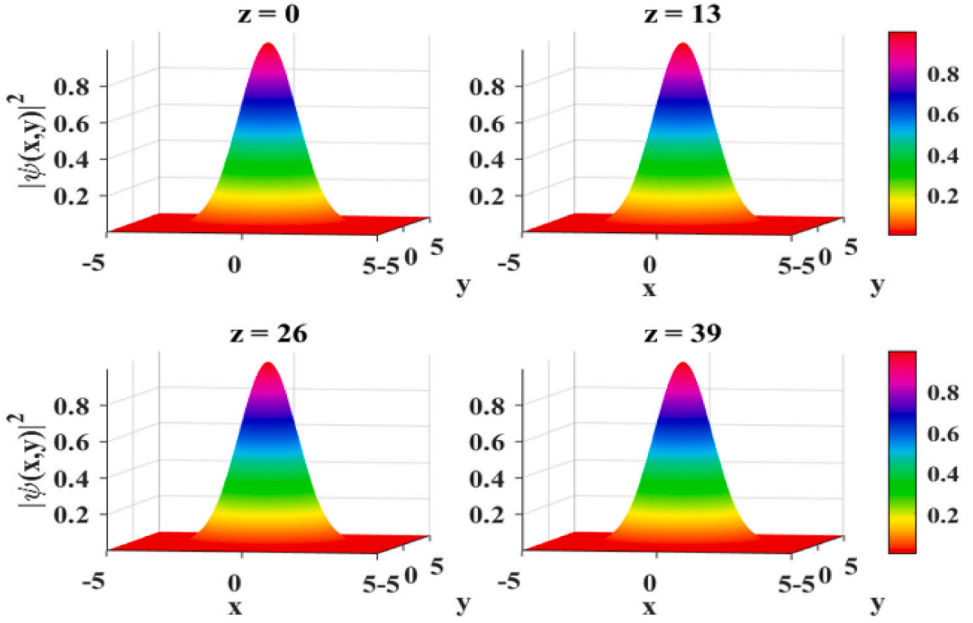

(a) Stable beam profile in the absence of gradient and potential terms

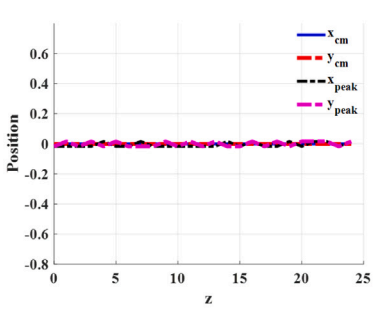

(b) The centroid and peak position of the intensity distribution

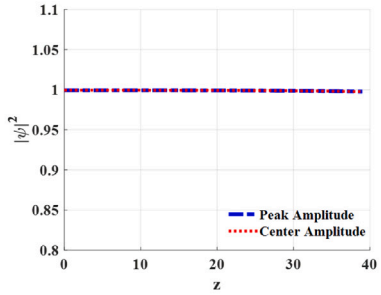

(c) The peak amplitude and the on-axis amplitude of the intensity distribution

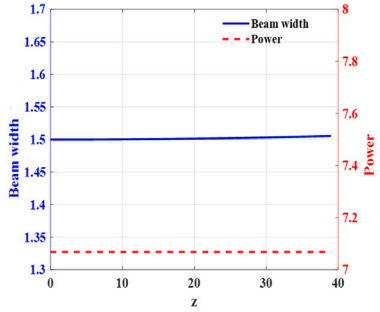

(d) The effective beam width $a(z)$ and the total beam power $P(z)$

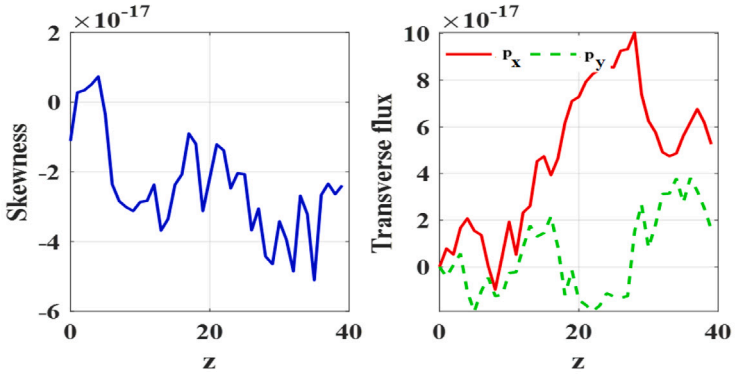

(e) Skewness and Poynting vector of stable beam propagation

Fig. 1. Evolving 2D nonlinear optical beam at $\zeta = 1$, $b = 1.5$, $G_3 = 0.06$ and $s = 0$.

To quantify the spatial localization of the beam during propagation, we compute both the centroid and the peak position of the intensity distribution and shown in Fig. 1(b). For a field amplitude ψ, and $P(z) = \iint |\psi(x, y, z)|^2 \, dx \, dy$, the beam centroid (center of mass) along each transverse direction is obtained as the first normalized moments of the intensity profile where, $x_{cm} = \frac{1}{P(z)} \iint x|\psi(x, y, z)|^2 \, dx \, dy$ and $y_{cm} = \frac{1}{P(z)} \iint y|\psi(x, y, z)|^2 \, dx \, dy$. These quantities describe the average position of the beam and therefore reveal any net transverse drift induced by nonlinearity, nonlinear gradient, or gain–loss imbalance. The peak position,

Fig. 1(b), is defined as the coordinates of the maximum intensity point, (x_{peak}, y_{peak}) which tracks the instantaneous location of the brightest spot within the beam. For a symmetric Gaussian input, the centroid and peak coincide initially, but they may diverge during evolution if the profile develops asymmetry or if the peak shifts relative to the overall energy distribution. When $s = 0$ centroid and peak positions remain locked at the origin throughout the propagation. This confirms that the beam stays perfectly centered, with no transverse drift or displacement. Fig. 1(c) displays the evolution of the peak amplitude, $\max_{x,y} |\psi(x, y, z)|^2$, and the on-axis amplitude, $|\psi(0, 0, z)|^2$, as a function of propagation distance z. Both quantities remain nearly constant and equal to unity throughout propagation. This behavior follows from the conservation of beam symmetry and the absence of gradient induced shift or any potential. Since the Gaussian input retains its centered profile and no additional phase tilt is introduced, the intensity maximum stays fixed at the beam center, leading to identical evolution for the peak and center amplitudes.

Fig. 1(d) shows the evolution of the effective beam width $a(z)$ and the total beam power $P(z)$. The power conserved during propagation, consistent with the conservative nature of the cubic nonlinear Schrödinger dynamics without gain/loss. The beam width remains nearly constant at the initial Gaussian value $a(0) = 1.5$. The slight breathing observed is attributed to the balance between diffraction and cubic nonlinearity. Together, the constant power and nearly invariant beam width confirm that the propagation is stable.

The variance (second moment) about the centroid is

$$\sigma_x^2(z) = \frac{1}{P(z)} \iint \left(x - x_{\mathrm{cm}}(z)\right)^2 |\psi(x, y, z)|^2 \, dx \, dy. \tag{3}$$

$x_{cm}(0)\&y_{cm}(0) = 0$ gives

$$\sigma_x^2(0) = \frac{1}{P} \iint x^2 A^2 \exp\left(-\frac{(x^2 + y^2)}{a^2}\right) dx \, dy. \tag{4}$$

During propagation, nonlinear focusing or diffraction causes σ to decrease or increase, so tracking it provides a direct measure of beam broadening or compression. While σ quantifies the width, it does not reveal whether the profile is symmetric. To detect asymmetry, we evaluate the third normalized central moment, or skewness:

$$Sk_x(z) = \frac{1}{P(z)\,\sigma_x^3(z)} \iint \left(x - x_{\mathrm{cm}}(z)\right)^3 |\psi(x, y, z)|^2 \, dx \, dy. \tag{5}$$

For the Gaussian input profile, both Sk_x and Sk_y vanish since the integrands are odd functions whose integrals over symmetric limits cancel. Hence, the input beam is symmetric along both transverse axes, and any departure from zero skewness during propagation provides a direct measure of asymmetry induced by nonlinear effect. The skewness of the system which is given in Fig. 1(e) has vanishingly small value and indicate nontilt beam propagation.

The transverse Poynting vector components are obtained by integrating the local flux densities over the transverse plane. They are defined as

$$p_x(z) = \iint S_x(x, y, z) \, dx \, dy, \qquad p_y(z) = \iint S_y(x, y, z) \, dx \, dy, \tag{6}$$

with

$$S_x(x, y, z) = \frac{i}{2}\left(\psi \, \partial_x \psi^* - \psi^* \, \partial_x \psi\right), \qquad S_y(x, y, z) = \frac{i}{2}\left(\psi \, \partial_y \psi^* - \psi^* \, \partial_y \psi\right). \tag{7}$$

Since

$$\psi \, \partial_x \psi^* - \psi^* \, \partial_x \psi = -2i \, \Im\left(\psi^* \partial_x \psi\right), \tag{8}$$

and similarly for the y-direction, the flux simplifies to

$$S_x = \Im(\psi^* \partial_x \psi), \qquad S_y = \Im(\psi^* \partial_y \psi). \tag{9}$$

For the Gaussian input beam, $\psi(x, y, 0)$ is real and symmetric, and the derivatives $\partial_x \psi$ and $\partial_y \psi$ are also real functions. Therefore $\psi^* \partial_x \psi$ and $\psi^* \partial_y \psi$ are purely real, making their imaginary parts vanish. As a result, $S_x = S_y = 0$ pointwise, and the integrated fluxes $p_x(z)$ and $p_y(z)$ remain zero during propagation. This confirms that, in the absence of gradient ($s = 0$), the beam carries no net transverse energy flow and its centroid remains fixed at the origin as in Fig. 1(e).

In the absence of gradient and potentials, the collision of two counter-propagating Gaussian beams serves as a reference benchmark for nonlinear interaction in two dimensions. At $z = 0$, two well-separated beams are launched symmetrically about the origin. As they propagate, diffraction and cubic self-focusing drive the beams toward each other, leading to overlap and compression. A sharp intensity peak is reached around $z \approx 300$, marking the collision point as shown in Fig. 2. Following this interaction, the beams re-emerge with profiles similar to their initial shape, indicating a quasi-elastic collision.

The collision dynamics is quantified in Figs. 3(a–e). Panel (a) shows the evolution of beam in the x–z plane at $y = 0$, clearly revealing the approach, overlap, and separation of the beams. Panel (b) plots the maximum intensity during propagation, which exhibits a sharp peak at the collision point. The shaded regions highlight pre- and post-collision intervals; the nearly equal peak levels indicate that the beams largely recover after interaction. Panel (c) shows the beam widths along x and y, $a_x(z)$ and $a_y(z)$, together with the total power $P(z)$. The power remains conserved throughout, confirming the conservative nature of the cubic nonlinear Schrödinger dynamics. The beam width exhibits a transient reduction at the collision, particularly along x (the collision axis), while $a_y(z)$ remains almost unaffected. Panel (d) compares lineouts along $y = 0$: initially two separate lobes merge at collision

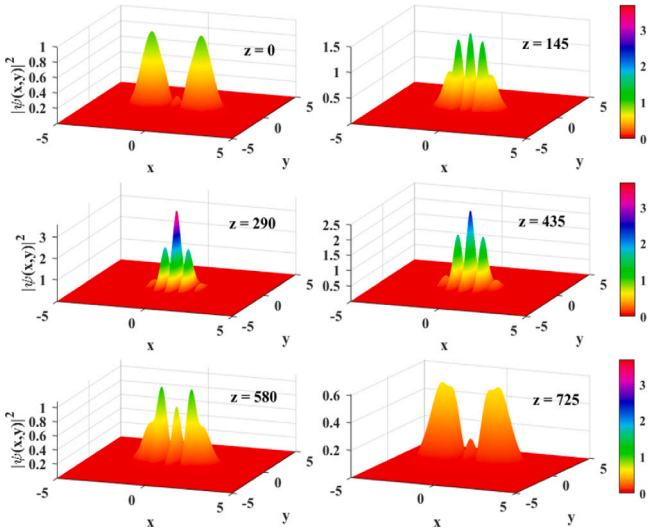

Fig. 2. Collision dynamics of two counter-propagating Gaussian beams at $\zeta = 1$, $b = 1.5$, $G_3 = 0.06$ and $s = 0$.

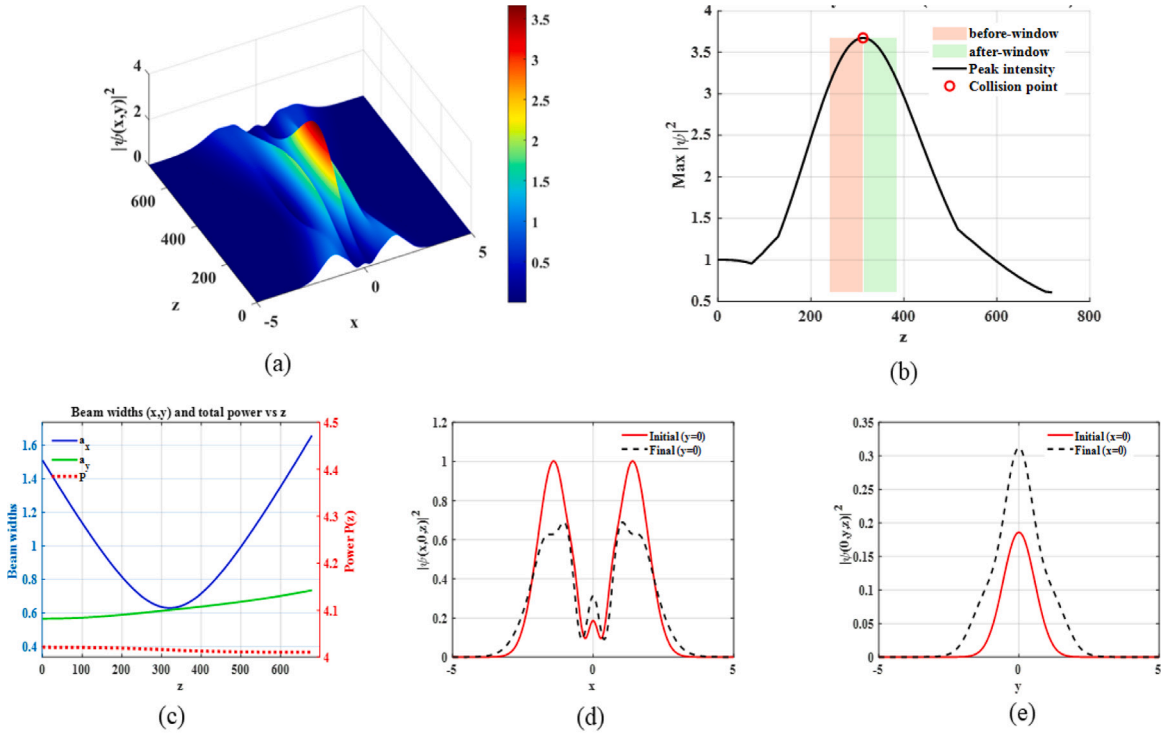

(a) System parameter evolution during collision of beams $s = 0$ at $\zeta = 1$, $b = 1.5$, $G_3 = 0.06$

Fig. 3. At $\zeta = 1$, $b = 1.5$, $G_3 = 0.06$, (a) Intensity $|\psi(x, 0, z)|^2$ in the x–z plane at $y = 0$, showing the beams approaching, colliding, and separating. (b) Evolution of the maximum intensity, highlighting the collision point (red circle) and shaded pre-/post-collision windows. (c) Beam widths $a_x(z)$ and $a_y(z)$ together with the conserved total power $P(z)$, showing transient compression in the x-direction during collision. (d) Lineouts of intensity along $y = 0$, comparing initial and final beam profiles; the two input lobes survive the collision but with slight reshaping. (e) Lineouts along $x = 0$, demonstrating broadening in the y-direction due to transverse energy redistribution.

and re-emerge with slight reshaping. Panel (e) shows the orthogonal cut along $x = 0$, which broadens after collision, indicating energy redistribution in the transverse direction. Together, these results demonstrate that the two-beam interaction is symmetric, power conserving, and nearly elastic, with only minor reshaping.

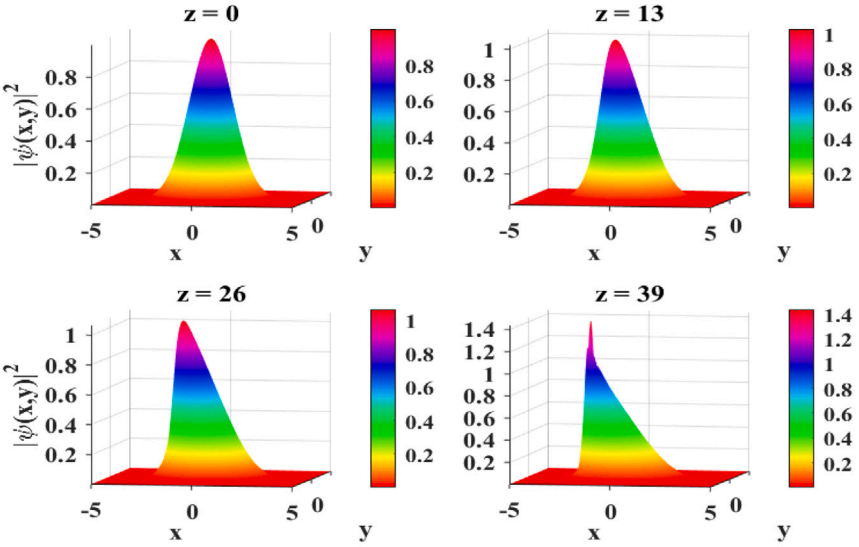

(a) Asymmetric drifting of beam profile at $s = 2.8$

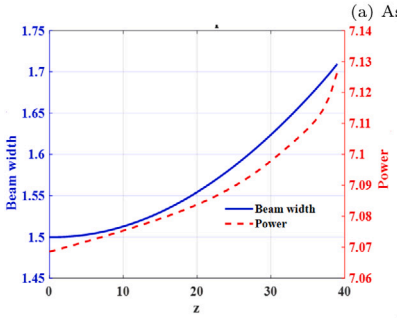

(b) Beam broadening with conserved power ensures that energy is redistributed.

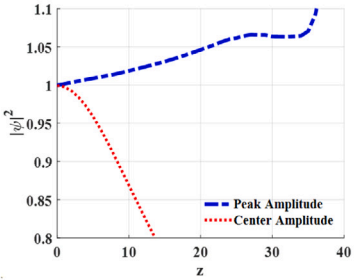

(c) Divergence between the peak and center amplitudes

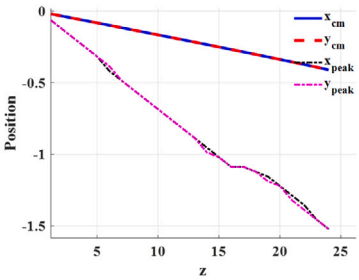

(d) Centroid and peak positions of the beam profile drift away from the origin

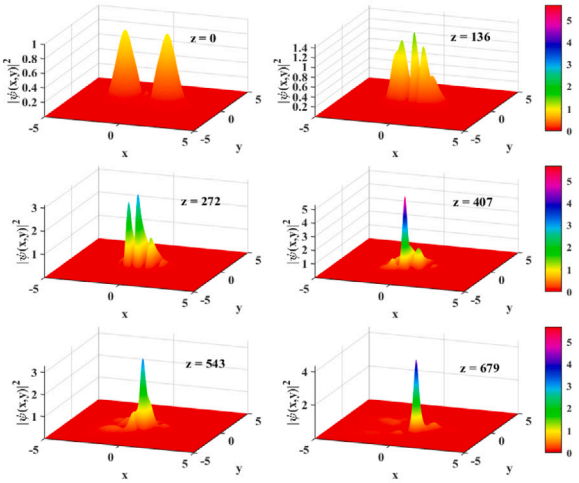

(e) Collision, localization, and reshaping of beam profile.

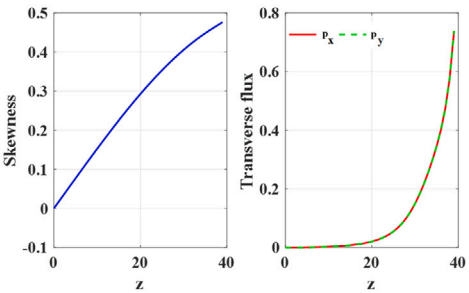

(f) The growth of skewness and transverse fluxes, confirming the emergence of asymmetric beam profiles

Fig. 4. Asymmetric beam profile in nonlinear media at $\zeta = 1$, $b = 1.5$, $G_3 = 0.06$, and $s = 2.8$.

In the presence of gradient asymmetry, $s = 2.8$, the propagation dynamics deviate strongly from the symmetric behavior. As shown in Fig. 4(a), the beam snapshots reveal how the initial Gaussian profile evolves asymmetrically, with the peak intensity shifting off-center and sharper gradients forming on one side of the beam. This distortion arises from the steepening-induced intensity-dependent current, which redistributes energy across the transverse plane.

Global diagnostics provide quantitative confirmation of this behavior. In Fig. 4(b), the beam width is seen to increase steadily, while the conserved power ensures that energy is redistributed rather than lost. At the same time, Fig. 4(c) shows a divergence between the peak and center amplitudes: the central value decays while the maximum shifts outward. This shift is reflected in the centroid and peak positions plotted in Fig. 4(d), where a monotonic drift away from the origin indicates a net transport of energy in both transverse directions. Fig. 4(e) illustrate the collision of two Gaussian beams at $s = 2.8$. The beams experience significant reshaping as they propagate and overlap. Initially separated double peaks gradually approach and strongly interact, leading to the formation of sharp, highly localized spikes. At the collision point $z \approx 407$, the maximum intensity rises drastically, indicating strong energy concentration induced by nonlinear gradient asymmetry. Beyond this point, the beams fail to recover their initial shape and instead evolve into a single, highly localized structure, showing clear evidence of inelastic interaction. This inelasticity can be attributed to the interplay between cubic nonlinearity and the steepening term, which breaks the left–right symmetry of the interaction. The steepening effect enhances higher-order spatial derivatives, amplifying local intensity gradients and driving energy flow toward the beam center. As a result, the system departs from quasi-elastic behavior, and the beams collapse into a localized peak with residual radiation around it. Finally, Fig. 4(f) illustrates the growth of skewness and transverse fluxes, confirming the emergence of asymmetric beam profiles and directed energy flow. Together, these results demonstrate that the gradient nonlinearity transforms a symmetric beam into a dynamically evolving structure with broken symmetry.

3. Incorporation of $\mathcal{PT}$−symmetric index profiles into beam propagation

To mitigate the gradient-induced asymmetry that emerges during nonlinear beam evolution, the refractive index of the medium is engineered through a $\mathcal{PT}$-symmetric design. In this framework, a balanced distribution of gain and loss regions, represented by the imaginary part of the refractive index, compensates for the nonlinear drift induced by self-steepening, while the real part provides the necessary waveguiding structure for beam confinement. Together, these components establish a non-Hermitian environment in which the interplay between gain, loss, and diffraction enables controlled, symmetric beam propagation. The potential which governs the beam is given as,

$$S_x = \operatorname{sech}\left(\frac{x+x_0}{k}\right) + \operatorname{sech}\left(\frac{x-x_0}{k}\right), \tag{10}$$

$$O_x = \operatorname{sech}\left(\frac{x+x_0}{k}\right)\tanh\left(\frac{x+x_0}{k}\right) + \operatorname{sech}\left(\frac{x-x_0}{k}\right)\tanh\left(\frac{x-x_0}{k}\right), \tag{11}$$

$$S_y = \operatorname{sech}\left(\frac{y+y_0}{k}\right) + \operatorname{sech}\left(\frac{y-y_0}{k}\right), \tag{12}$$

$$O_y = \operatorname{sech}\left(\frac{y+y_0}{k}\right)\tanh\left(\frac{y+y_0}{k}\right) + \operatorname{sech}\left(\frac{y-y_0}{k}\right)\tanh\left(\frac{y-y_0}{k}\right), \tag{13}$$

$$V_r(x,y) = V_0\left(S_y S_x\right)^2, \qquad V_i(x,y) = W_0\left(O_y S_x + S_y O_x\right), \tag{14}$$

$$V = V_r + iV_i \tag{15}$$

$V_r(x,y)$ is even in both x and y, while $V_i(x,y)$ is odd under $(x,y) \mapsto (-x,-y)$. Hence the overall potential satisfies the $\mathcal{PT}$−symmetry condition

$$V_r(x,y) = V_r(-x,-y), \quad V_i(x,y) = -V_i(-x,-y). \tag{16}$$

V_0 sets the strength of the real index modulation, x_0/y_0 and k control the potential well separation and localization width, and W_0 defines the gain–loss amplitude. This specific potential considered here is not unique. It is adopted as a representative example of a smooth, spatially localized gain–loss distribution that satisfies the $\mathcal{PT}$−symmetry condition. Other $\mathcal{PT}$−symmetric or non-Hermitian index profiles may lead to qualitatively similar stabilization effects, which can have scope for future studies.

The governing MNLS equation is expressed as:

$$\begin{aligned} &i\frac{\partial}{\partial z}\psi(x,y,z) + \zeta\nabla_\perp^2\psi(x,y,z) + \beta_1(x,y)|\psi(x,y,z)|^2\psi(x,y,z) + \left(V_r(x,y) + iV_i(x,y)\right)\psi(x,y,z) + \\ &is\left(\frac{\partial}{\partial x} + \frac{\partial}{\partial y}\right)\left(|\psi(x,y,z)|^2\psi(x,y,z)\right) = 0, \end{aligned} \tag{17}$$

To quantify the internal redistribution of the energy, we examine the total beam power, and its evolution rate, dP/dz, which is theoretically related to the overlap integral.

$$\frac{dP}{dz} = \iint \frac{\partial}{\partial z}(\psi^*\psi)dxdy, \tag{18}$$

$$\frac{dP}{dz} = \iint \left(\psi^*\frac{\partial\psi}{\partial z} + \psi\frac{\partial\psi^*}{\partial z}\right)dxdy. \tag{19}$$

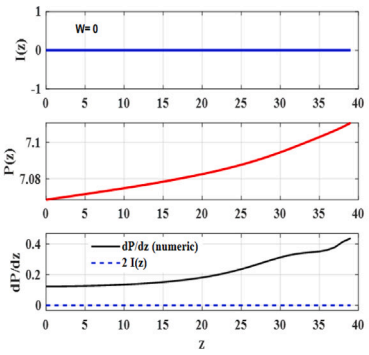

(a) For $W_0 = 0$, $I(z)$ nearly zero and $P(z)$ approximately constant, indicates a system with no external power coupling.

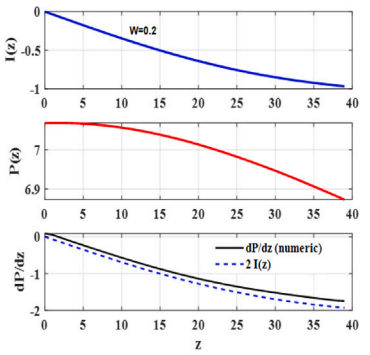

(b) For $W_0 = 0.2$, $I(z)$ becomes negative and $P(z)$ decreases, signifying loss-dominated propagation.

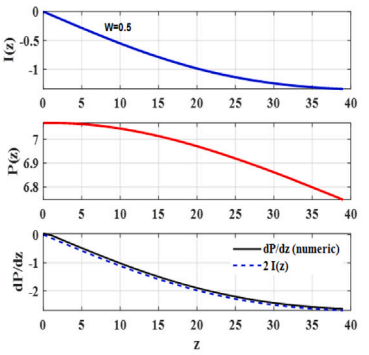

(c) For $W_0 = 0.5$, $I(z)$ becomes negative and $P(z)$ decreases, signifying loss-dominated propagation.

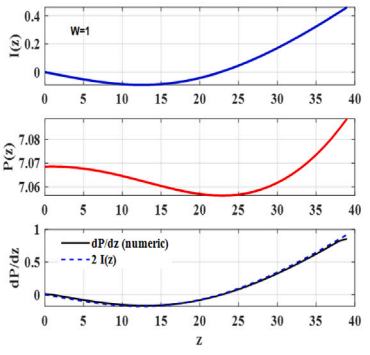

(d) For $W_0 = 1$, $I(z)$ changes sign and $P(z)$ starts to recover, demonstrating the onset of gain-loss compensation.

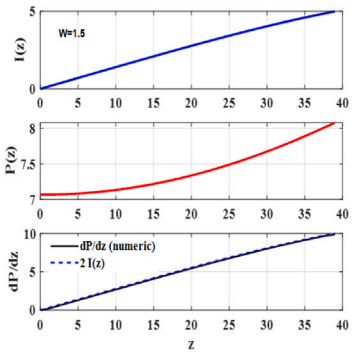

(e) For $W_0 = 1.3$, $I(z)$ and $P(z)$ increases demonstrating the instability of beam propagation.

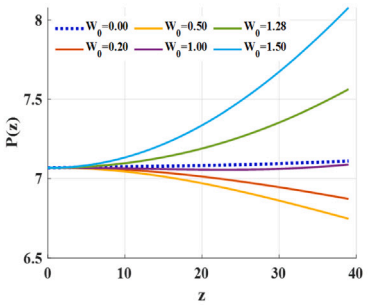

(f) The power remains conserved for W_0=0, decreases for weak W_0, and increases for large W_0, indicates the transition from loss-dominated to gain-dominated regimes.

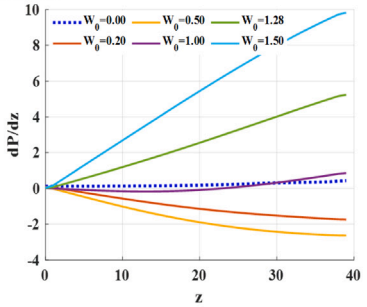

(g) Evolution of the longitudinal power rate dP/dz for different W_0.Variation of power nearly zero for $W_0 = 0$, and decreases/increases as W_0 decreases/increases

Fig. 5. Evolution of the overlap integral $I(z)$ (top), total beam power $P(z)$ (middle), and its propagation derivative dP/dz (bottom) for different values of the imaginary potential strength W_0 at $\zeta = 1$, $b = 1.5$, $k = 1.5$, $G_3 = 0.06$, and $s = 2.8$.

Substitute the governing MNLS equation into this evolution equation for the total power variation. The diffraction term and the nonlinear-gradient contribution come as total spatial derivative terms. Upon integration over the entire transverse plane, these contributions vanish due to the imposed boundary conditions,

$$\psi \to 0, \quad \nabla\psi \to 0 \quad \text{as} \quad |(x, y)| \to \infty,$$

which are satisfied by localized beam solutions. Consequently, the net power variation is entirely determined by the imaginary part of the $\mathcal{PT}$-symmetric potential. Therefore, the quantity $I(z)$ serves as a direct measure of the gain–loss exchange between the propagating optical beam and the surrounding medium.

$$\frac{dP}{dz} = 2I(z) \quad \text{where} \quad I(z) = \iint V_i(x, y)|\psi|^2 dx dy \tag{20}$$

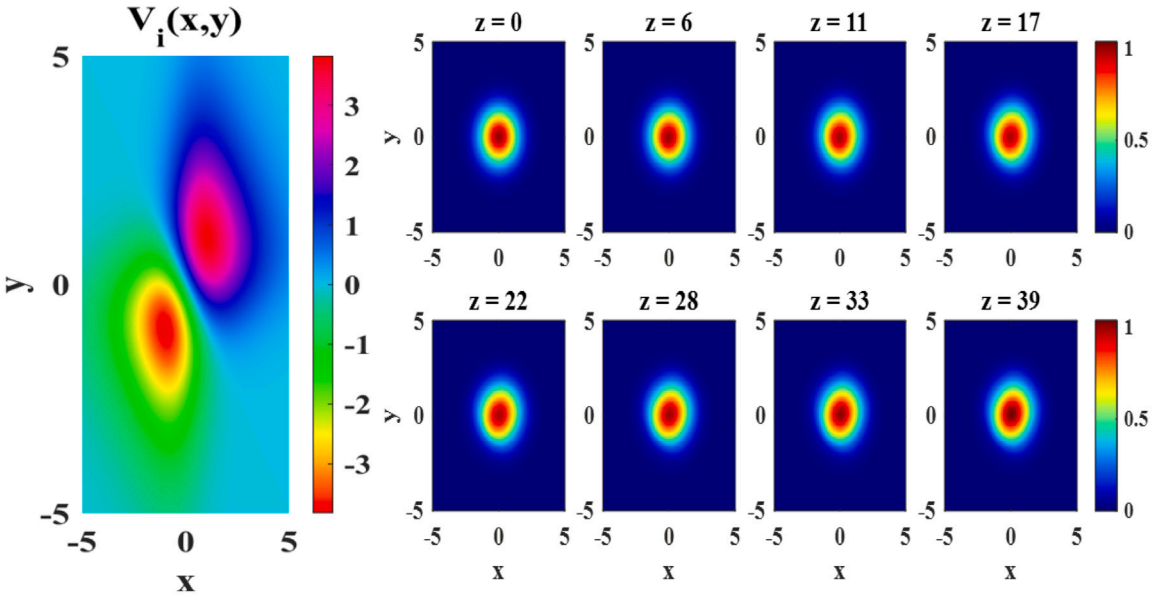

(a) $x_0 = y_0 = 0.2$, $k = 1.5$ and $W_0 = 1.28$

(b) $s = 2.8$, $x_0 = y_0 = 0.2$, $k = 1.5$ and $W_0 = 1.28$

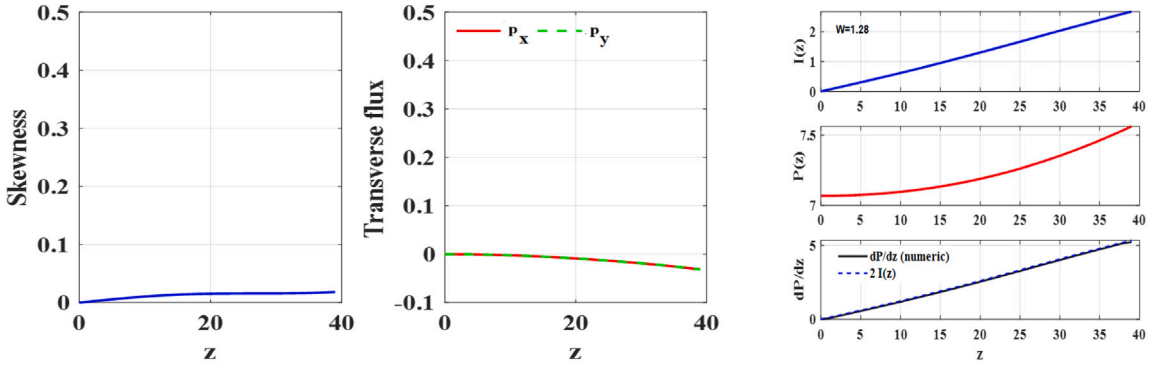

(c) Skewness and transverse flux evolution, where both quantities remain close to zero at $s = 2.8$, $x_0 = y_0 = 0.2$, $k = 1.5$ and $W_0 = 1.28$

(d) $I(z)$ and $P(z)$ increases slightly, but the beam drift canceled

Fig. 6. (a) Imaginary part of the $\mathcal{PT}$−symmetric potential (b) Evolution of the transverse intensity distribution showing that the $\mathcal{PT}$-symmetric gain–loss profile sustains a symmetric and localized beam. (c) Skewness and transverse flux evolution, where both quantities remain close to zero, indicating suppression of asymmetry and balanced energy flow. (d) Evolution of propagation derivative of non steepening beam.

Here, $I(z)$ measures the net power exchange between the beam and the imaginary component of the field. Figs. 5(a–e) display $I(z)$, $P(z)$, and dP/dz for various W_0 values, highlighting how the balance between nonlinear flux and gain/loss determines beam stability.

For $W_0 = 0$, $I(z)$ remains nearly zero and $P(z)$ approximately constant, indicating a conservative system with no external energy coupling. For low gain/loss strength ($W_0 = 0.2$–0.5), $I(z)$ remains negative throughout propagation, signifying dominant loss and a gradual decay of total power. The derivative dP/dz closely follows $2I(z)$, confirming that the reduction in $P(z)$ originates from consistent power leakage.

For the intermediate gain–loss strength $W_0 = 1$, where the competing effects of gain and loss almost balance each other, $I(z)$ exhibits a nonmonotonic evolution—initially negative, reflecting weak attenuation, and later positive as the gain becomes more influential. Consequently, $P(z)$ first decreases slightly and then recovers, forming a shallow minimum at the point where $I(z)$ changes sign. The close agreement between the numerically computed dP/dz and the analytical $2I(z)$ confirms that the power exchange follows the expected conservation relation. Physically, this case represents the transition threshold: asymmetry–induced energy flux is nearly counteracted by the imaginary index modulation, resulting in a state of marginal energy exchange and minimal beam distortion. Moreover, variation of the power is much less.

Beyond this regime (e.g., $W_0 \approx 1.3$), $P(z)$ and dP/dz increases, as shown in Figs. 5(f–g), demonstrating the instability of beam propagation. The underlying mechanism for stable beam propagation is clear here. The nonlinear-gradient term generates an internal transverse energy flux that simultaneously drives beam drift and redistributes optical power away from the beam center, with a

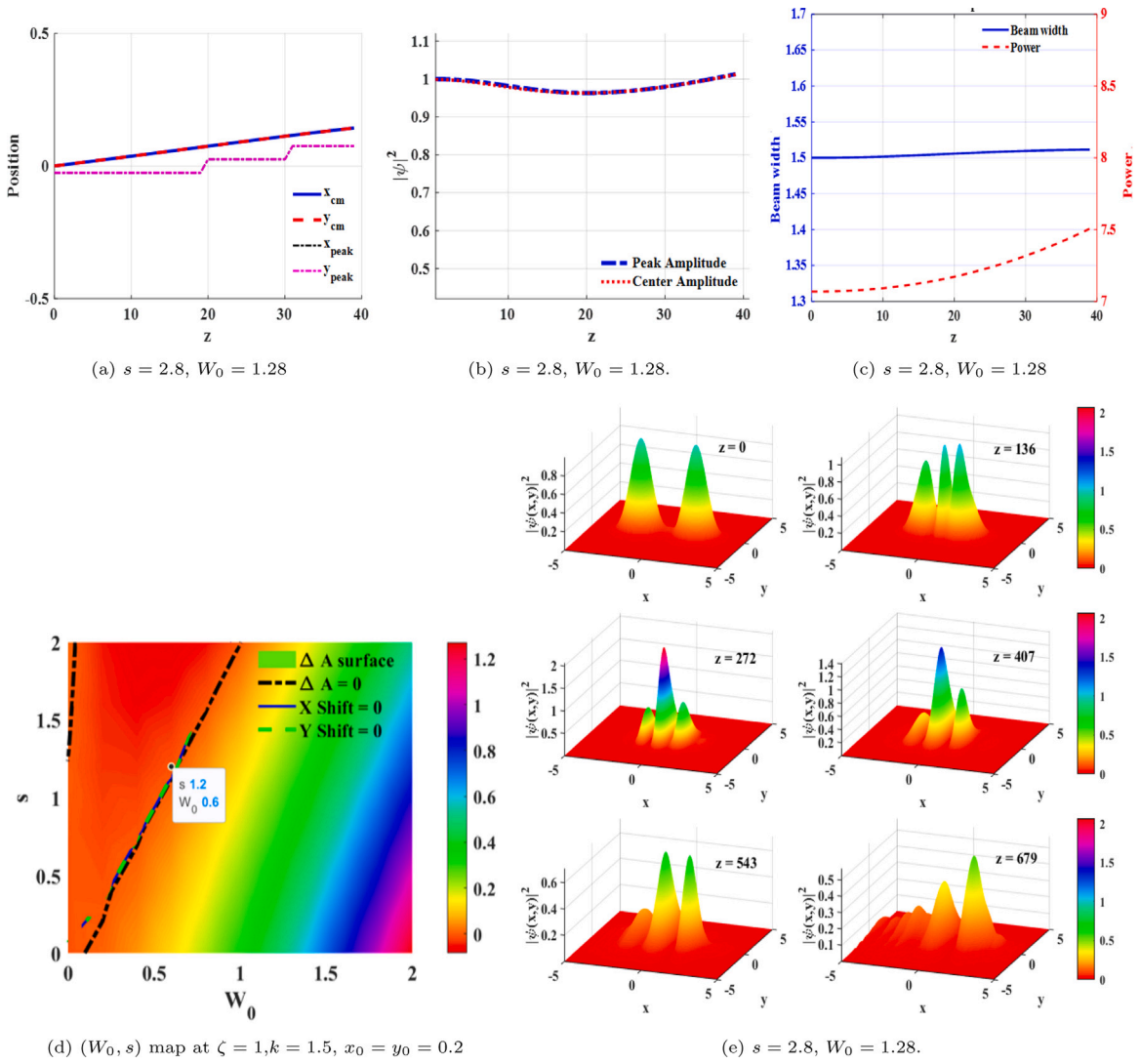

(a) $s = 2.8$, $W_0 = 1.28$ (b) $s = 2.8$, $W_0 = 1.28$. (c) $s = 2.8$, $W_0 = 1.28$

(d) (W_0, s) map at $\zeta = 1, k = 1.5$, $x_0 = y_0 = 0.2$ (e) $s = 2.8$, $W_0 = 1.28$.

Fig. 7. Statistical measures of the beam: (a) centroid and peak positions (b) peak and center amplitudes (c) beam width with total power. The near coincidence of centroid and peak, along with confined width and stable amplitude, confirms robust beam propagation in the balanced $\mathcal{PT}$-symmetric regime. (d) Stability characteristics of the two-dimensional beam in the (W_0, s) plane. (e) Dynamical regulation of energy flow in $\mathcal{PT}$-symmetric regime during collision of beams.

strength that scales with the self-steepening parameter s. The antisymmetric imaginary component of the $\mathcal{PT}-$symmetric potential introduces an external gain–loss-induced flux of opposite sign, whose magnitude is controlled by the parameter W_0. Because both contributions act as competing fluxes with monotonic dependence on , their cancellation occurs at a unique value of W_0 and s, giving rise to the observed one-to-one balance condition and the simultaneous suppression of transverse drift and amplitude variation.

For the potential, which is shown in Fig. 6(a), with $V_0 = 0$, and $W_0 = 1.28$, Fig. 6(b) demonstrates that the initial Gaussian evolves in a confined manner without exhibiting unbounded spreading or decay. Although the gradient nonlinearity tends to reshape the beam, the antisymmetric gain–loss distribution of the $\mathcal{PT}$-symmetric potential stabilizes the propagation, resulting in a nearly symmetric field that remains localized around the origin throughout the evolution.

The beam statistics in Fig. 6(c) provide further evidence of this stabilization. The skewness remains close to zero, confirming the absence of strong asymmetry in the transverse intensity distribution. Similarly, the transverse fluxes p_x and p_y fluctuate near zero, reflecting the balanced inflow and outflow of energy inherent to $\mathcal{PT}-$symmetric configurations. $I(z) > 0 \rightarrow$ hence $dP/dz > 0$ as shown in Fig. 6(d), which means the total power increases gradually along propagation. Even though visually the beam looks stationary (no drift, no deformation), the imaginary component of the potential continues to provide a net gain flux toward the beam center. But, this does not indicate instability — it is a marginally amplifying steady state.

The centroid positions (x_{cm}, y_{cm}) and the peak positions $(x_{\text{peak}}, y_{\text{peak}})$ in Fig. 7(a) stay close to the beam center with only minor oscillations, showing that the potential suppresses drift and traps the beam in a stationary regime. The peak and central amplitudes shown in Fig. 7(b) evolve in phase, indicating that no secondary off-axis maxima develop during propagation.

The beam width $a(z)$ remains nearly constant, while the total power $P(z)$ undergoes a controlled increase as in Fig. 7(c). Fig. 7(d) illustrates the stability characteristics of the two-dimensional beam in the (W_0, s) plane. The color shading encodes the amplitude variation ΔA, while the black dashed curve traces the set of points where $\Delta A = 0$, signifying energy balance between asymmetry and $\mathcal{PT}$−symmetric gain/loss. In parallel, the green and blue contours correspond to vanishing centroid displacement along the x- and y-axes, respectively. The points where these curves intersect highlight parameter pairs (W_0, s) at which the beam preserves both its amplitude and spatial location, thus realizing a completely stabilized state. The map demonstrates that for a given s, two W_0 values can nullify amplitude variation, but only one of them simultaneously removes transverse drifts in both directions. This dual condition is more restrictive in two dimensions, as stability requires suppression of motion along both x and y axes in addition to conserving power. For example, the coordinate $(W_0 = 0.6,\ s = 1.2)$ represents such a balance point, where the flux arising from steepening gradients is counteracted by the $\mathcal{PT}$−symmetric gain/loss profile, along with cancellation of centroid drift. Overall, the diagram delineates regions of partial balance (amplitude-conserved but drifting beams) from the narrow curve corresponding to fully trapped and stable 2D localized states. Moreover, as the asymmetry parameter increases, the imaginary potential coefficient, which balances the beam, increases.

The collision sequence between the beams also reveals that the $\mathcal{PT}$−induced gain/loss balance dynamically regulates the energy flow and prevents unidirectional drift and suppresses the formation of steep intensity gradients, leading to a quasi-reversible collision process even in a strongly nonlinear, self-steepening regime. The narrowing of beam corresponds to the approach and overlap of the beams, while its subsequent broadening marks their separation after interaction. This has been shown in Fig. 7(e). The comparative collision dynamics observed in the three cases ($s = 0$, $s \neq 0$, and the balanced s–W_0 configuration) demonstrate that, while gradient nonlinearity alone enhances asymmetry and deformation during interaction, the balanced configuration enables solitons to recover their profiles after collision. This behavior indicates that the stabilization mechanism is robust rather than accidental and is not limited to ideal single-beam propagation, but remains effective during beam–beam interactions.

To systematically identify the potential shapes that compensate the asymmetry, we mapped the potential width parameter (k) (which controls the transverse localization of the imaginary profile) as a function of s in Fig. 8(a). Three loci in the (s, k)-plane, $\Delta A = 0, x_{shift} = 0, y_{shift} = 0$ denote potential widths that exactly counterbalance both the amplitude change and centroid drift for the given s at $W_0 = 0.4$. The monotonic decrease of k with s indicates that stronger asymmetry requires more tightly localized imaginary potentials to restore balance. The near-coincidence of the three curves over much of the diagram demonstrates that amplitude and positional balance can be achieved simultaneously for a single potential shape. When the curves diverge, separate tuning of amplitude and centroid conditions are required. Intersection points (marked in the plot) therefore identify practical design targets for experimental realization where both energetic and spatial equilibria are met.

Fig. 8(b) illustrates the combined influence of the potential offset parameters (x_0, y_0) and s on the balancing imaginary potential coefficient $W_0 = 0.4$. Stabilization condition achieved by $W_0 = 0.4$ is for $s = 0.8$ and $x_0 = y_0 = 0.2$. As the separation parameters x_0 and y_0 increase, the centers of the gain and loss regions in the $\mathcal{PT}$-symmetric potential move farther away from the beam's intensity maximum, thereby reducing the spatial overlap between the optical field and the regions where energy exchange occurs. Consequently, a higher gain/loss strength W_0 is required to achieve the same level of balance between the nonlinear self-steepening-induced energy flow and the compensating $\mathcal{PT}$-induced flux. This trend is consistent across all values of s: for larger asymmetry coefficients, the nonlinear gradient pushes energy outward more strongly, and thus the system demands proportionally higher W_0 values to restabilize the beam. In summary, the figure demonstrates that both increasing the potential separation (x_0, y_0) and enhancing the derivative nonlinearity strengthen the requirement for a larger imaginary potential amplitude to maintain stationary propagation without drift or distortion.

The diffraction coefficient is another control knob, which reduces the transverse gradients and smoothens the intensity profile like the imaginary potential. As ζ increases, the natural spreading of the beam becomes more pronounced, which smooths the sharp intensity gradients responsible for the derivative nonlinearity-induced drift. Consequently, the nonlinear energy flux that tends to drive the beam outward from its center becomes weaker, and a smaller imaginary potential is sufficient to counterbalance it, as shown in Fig. 8(c). This inverse dependence W_0 on ζ reveals that stronger diffraction enhances the system's ability to restore spatial symmetry. However, Fig. 8(d) shows that this stabilization comes at the cost of reduced peak amplitude. With higher diffraction, the beam expands transversely, and its central intensity decreases because the total optical power is redistributed over a broader region. Thus, increasing diffraction effectively suppresses the self-steepening-driven beam shift but cannot recover the lost intensity, leading to a spatially balanced yet energetically weakened beam.

When the real potential is gradually introduced, the system exhibits periodic oscillations in the beam amplitude during propagation as in Figs. 8(f)–(h). This behavior arises from the interplay between the confining effect of the real potential and the spreading tendency due to diffraction. Initially, the real potential focuses the beam, increasing its amplitude; as the field becomes highly localized, diffraction becomes dominant, pushing energy outward and lowering the peak. This focusing–defocusing cycle repeats, producing amplitude oscillations around a quasi-equilibrium state. Thus, while the drift is suppressed primarily by diffraction, the inclusion of the real potential introduces breathing-type amplitude modulation, reflecting a dynamic balance between potential trapping and diffractive broadening.

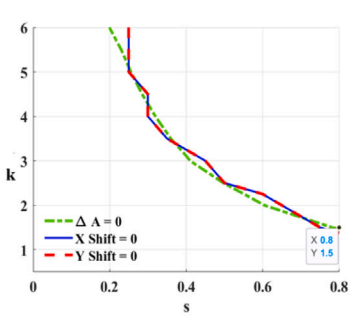

(a) Larger steepening requires a more localized potential (smaller k) to maintain spatial and/or energetic balance

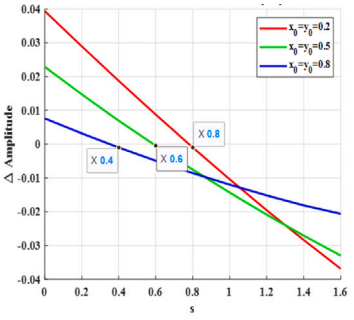

(b) Dependence of s on the potential offset parameters (x_0, y_0) for the condition $\Delta A = 0$.

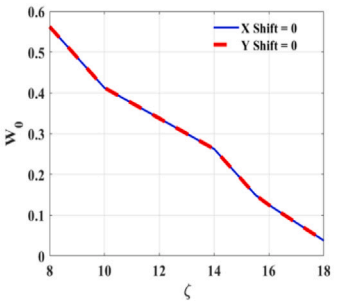

(c) Variation of imaginary potential which balance the beam with diffraction at $s = 1.4$, $V_0 = 0$

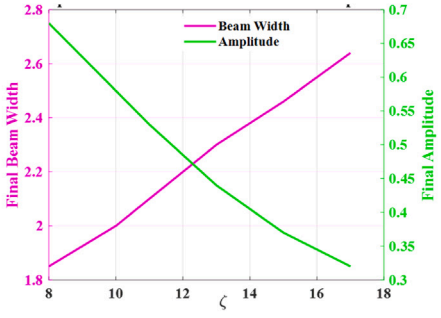

(d) $s = 1.4$, $V_0 = 0$

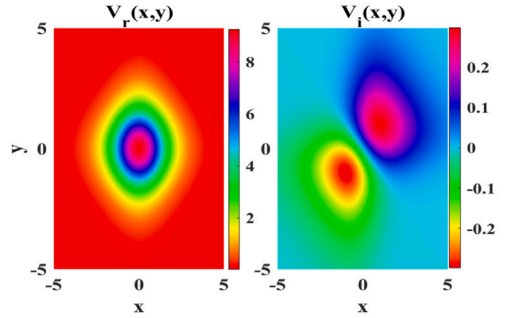

(e) $V_0 = 0.6$,$W_0 = 0.1$, $x_0 = y_0 = 0.2$, $k = 1.5$

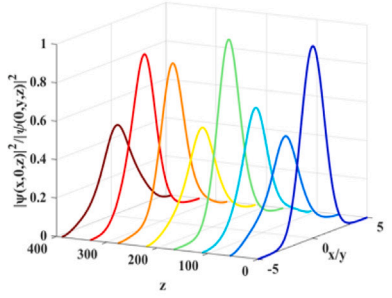

(f) $s = 2.8$, $W_0 = 0.1$, $V_0 = 0.6$

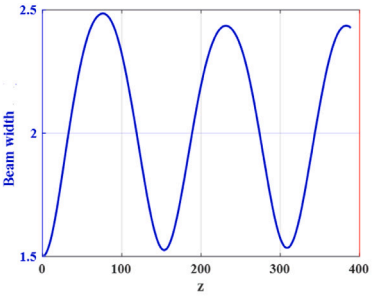

(g) $s = 2.8$, $W_0 = 0.1$, $V_0 = 0.6$

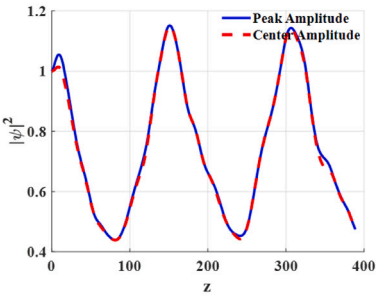

(h) $s = 2.8$, $W_0 = 0.1$, $V_0 = 0.6$

Fig. 8. (a): Parameter tuning for stabilized propagation without amplitude variation and beam shift at (a): $W_0 = 0.4$, $x_0 = y_0 = 0.2$ (b): $W_0 = 0.4$, $k = 1.5$ (c): At $x_0 = y_0 = 0.2$ variation of balancing potential with diffraction (d): Final beam width and amplitude as function of ζ. (e): Potential distribution at $V_0 = 0.6$, $W_0 = 0.1$, $x_0 = y_0 = 0.2$, $k = 1.5$. (f)–(h) Effect of increasing real potential depth V_0 on soliton propagation for $s = 2.8$ and $W_0 = 0.1$ and $\zeta = 18$.

4. Perturbation analysis and growth-rate evaluation

Perturbation analysis provides a fundamental tool for assessing the dynamical stability of soliton solutions. In real optical systems, solitary waves are subject to unavoidable fluctuations in refractive index, gain, loss, or nonlinear response. To test their robustness, a small complex perturbation $\delta\psi(x, y, z)$ is added to the initial field $\psi(x, y, z)$, and its evolution is monitored during propagation. If the perturbation amplitude $\|\delta\psi(z)\|$ increases exponentially with z, the soliton is unstable and will eventually deform or disintegrate. In contrast, when $\|\delta\psi(z)\|$ remains bounded or decays, the soliton is dynamically stable and can propagate over long distances.

To investigate the linear stability of nonlinear modes in the two-dimensional $\mathcal{PT}$−symmetric system, we consider a perturbed field $\psi(x, y, z) = \phi(x, y) + \delta\psi$, where ϕ is a localized reference profile and

$$\delta\psi(x, y, 0) = \epsilon\, \phi(x, y)\, \eta(x, y) + \epsilon\, \xi(x, y), \tag{21}$$

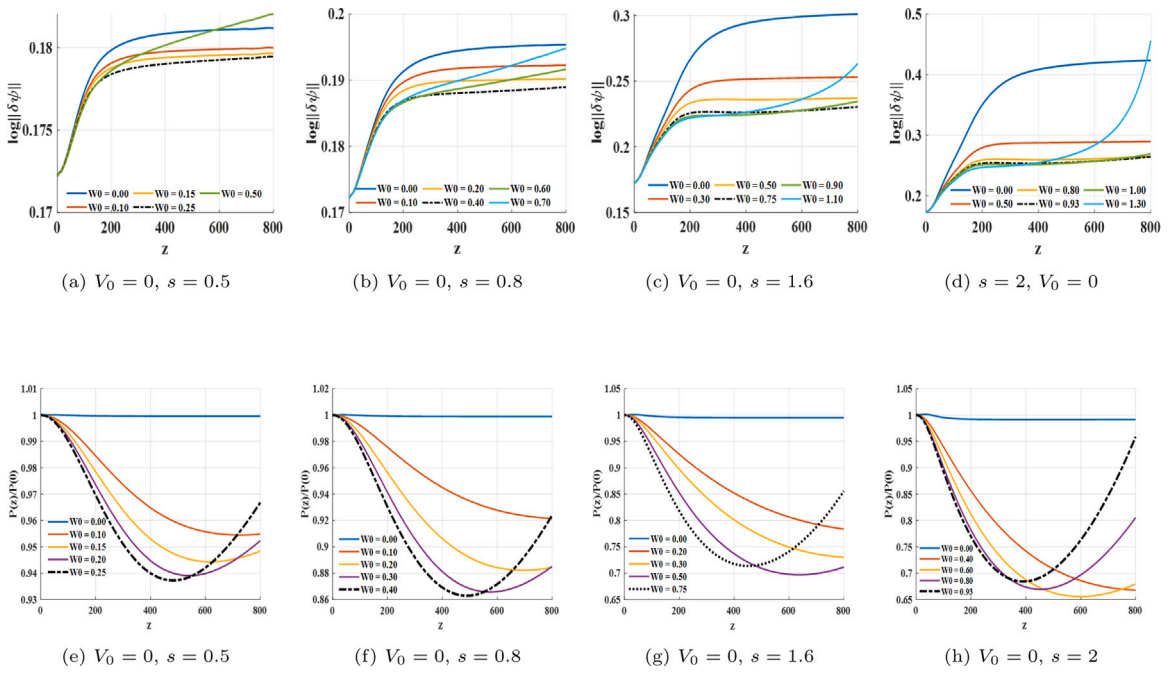

(a) $V_0 = 0,\ s = 0.5$ (b) $V_0 = 0,\ s = 0.8$ (c) $V_0 = 0,\ s = 1.6$ (d) $s = 2,\ V_0 = 0$

(e) $V_0 = 0,\ s = 0.5$ (f) $V_0 = 0,\ s = 0.8$ (g) $V_0 = 0,\ s = 1.6$ (h) $V_0 = 0,\ s = 2$

Fig. 9. (a)–(d): Evolution of the perturbation norm $\log\|\delta\psi(z)\|$ for different values of the gain–loss strength W_0 $\epsilon = 10^{-2}$. (e)–(h): Normalized power evolution $P(z)/P(0)$ for different values of the gain–loss amplitude W_0 with $\epsilon = 10^{-2}$. For small W_0, the power remains nearly constant, whereas larger W_0 introduces significant loss imbalance and power depletion during propagation.

with η, ξ being complex random fields of small amplitude and ϵ is small coefficient enhancing the perturbation. The evolution is governed by

$$i\frac{\partial\psi}{\partial z} = L[\psi] + N[\psi], \tag{22}$$

where L contains diffraction and the complex $\mathcal{PT}$-symmetric potential, and N contains the cubic nonlinearity and nonlinear gradient term.

Linearization around ϕ yields the Bogoliubov–de Gennes (BdG) system

$$i\frac{\partial}{\partial z}\begin{pmatrix}\delta\psi\\ \delta\psi^*\end{pmatrix} = \begin{pmatrix}L+M & A\\ -A^* & -(L+M)^*\end{pmatrix}\begin{pmatrix}\delta\psi\\ \delta\psi^*\end{pmatrix}, \tag{23}$$

where $M = (\partial N/\partial\psi)|_\phi$ and $A = (\partial N/\partial\psi^*)|_\phi$ arise from the derivatives of the nonlinear terms. The eigenvalues λ of Eq. (23) govern the perturbation dynamics, with $\Re(\lambda) > 0$ indicating growth.

In two spatial dimensions, the BdG matrix is prohibitively large and is therefore not constructed numerically. Instead, stability is assessed dynamically by evolving both a perturbed field ψ and an unperturbed reference field $\psi_{\text{un}} = \phi$ using a Crank–Nicolson scheme in which the linear operator is treated implicitly and the nonlinear terms explicitly. The instantaneous perturbation

$$\delta\psi(z) = \psi(z) - \psi_{\text{un}}(z) \tag{24}$$

is monitored during propagation. Because the initial random disturbance excites all BdG modes, its evolution can be written formally as

$$\delta\psi(z) = \sum_j c_j u_j e^{\lambda_j z}, \tag{25}$$

so that, in the linear regime, the dominant mode satisfies

$$\|\delta\psi(z)\| \sim e^{\Re(\lambda_{\max})z}. \tag{26}$$

Accordingly, the instability exponent is obtained by fitting a straight line to $\log\|\delta\psi(z)\|$ versus z, providing a dynamic estimate of the leading BdG growth rate without explicitly forming the BdG operator. The evolution of the perturbation norm $\|\delta\psi(z)\|$ which provides a clear dynamical signature of the stability of localized modes under variations of the imaginary potential strength W_0 is shown in Fig. 9. For each fixed value of the nonlinear gradient coefficient s, there exists a specific value of W_0 for which the perturbation norm remains minimal throughout propagation. For instance, when $s = 0.5$ the smallest perturbation growth occurs at approximately $W_0 \simeq 0.25$, while for $s = 0.8$ the balancing point shifts to about $W_0 \simeq 0.40$, for $s = 1.6$ $W_0 \simeq 0.75$ and for $s = 2$,

$W_0 \simeq 0.93$ and these values are in agreement with the unperturbed case discussed initially in Fig. 7(d). For values of W_0 either below or above this balancing point, the perturbation norm grows significantly faster. When W_0 is smaller than the balancing value, the imaginary potential is insufficient to counteract the nonlinear-gradient-induced transverse momentum, leading to a drift-type instability. This manifests as a steady increase in $\|\delta\psi(z)\|$. When W_0 exceeds the balancing value, the excess gain–loss asymmetry introduces an imbalance between the two sides of the localized mode, producing gain-induced deformation and again resulting in enhanced perturbation growth. Thus, both sides of the balancing point lead to stronger instability, and only a narrow interval of W_0 yields robust behavior.

The evolution of the beam power $P(z) = \int |\psi(x, y, z)|^2 \, dx \, dy$ provides an additional indicator of the dynamical balance in the $\mathcal{PT}$−symmetric system. For each value of s, the power curves exhibit a characteristic non-monotonic behavior near the balancing value of the gain–loss strength W_0. At this particular value (for example, $W_0 \approx 0.25$ when $s = 0.5$, and $W_0 \approx 0.40$ when $s = 0.8$), the power initially decreases slightly due to diffraction and the effective nonlinear loss induced by the self-steepening term, but after a short propagation distance it stabilizes and begins to increase. This turning point indicates that the imaginary potential has reached the exact strength needed to compensate the nonlinear-gradient-induced energy flow.

For W_0 below this balancing value, the gain is too weak to counteract the self-steepening and diffraction effects, leading to a monotonic decrease in the power throughout the evolution. In contrast, when W_0 is larger than the balancing value, the gain dominates, and the beam power grows rapidly from the beginning of the propagation. Thus, the non-monotonic behavior—initial decrease followed by increase—appears only at the unique value of W_0 where gain, loss, diffraction, and nonlinear-gradient effects are exactly balanced. This behavior complements the perturbation-norm analysis and provides a clear signature of the parameter regime in which stable $\mathcal{PT}$−symmetric soliton propagation is achieved.

The stability analysis employed here is based on the dynamical evolution of small-amplitude perturbations superimposed on stationary soliton solutions. Unlike a full Bogoliubov–de Gennes analysis, this approach does not yield the complete linear eigenvalue spectrum. However, it directly probes the dominant physically relevant instability channels and captures power redistribution and nonlinear feedback effects. The extracted growth rates can be regarded as reliable indicators of linear stability provided that the perturbations remain sufficiently small and the analysis is restricted to the initial exponential growth regime before nonlinear saturation sets in.

5. Conclusion

In this work, we have established a comprehensive framework for understanding and controlling the dynamics of self-steepening-induced asymmetric solitons in two-dimensional nonlinear media. By incorporating a $\mathcal{PT}$−symmetric complex refractive-index landscape into the modified nonlinear Schrodinger equation (MNLS), we demonstrated that the intrinsic gradient flows generated by the nonlinear gradient term can be counterbalanced through a carefully engineered distribution of gain and loss. Our systematic parameter scans revealed that the imaginary component of the potential plays the primary role in suppressing transverse drift, while diffraction and the real part of the potential assist in restoring amplitude and spatial confinement.

A key finding of this study is the existence of a unique balancing point for every self-steepening strength (s), characterized by a corresponding gain/loss coefficient (W_0), at which the beam's centroid remains pinned and the soliton maintains its shape. Increasing the diffraction coefficient (ζ)can reduce the drift even for small (W_0), but this alone cannot prevent the rapid decay of amplitude. Introducing the real potential modifies the transverse energy flow and leads to characteristic oscillations in peak amplitude — arising from intermittent dominance of diffraction, nonlinearity, and potential-induced focusing — which we interpreted as a nonlinear breathing behavior within a non-Hermitian landscape.

In addition to single-beam propagation, the robustness of the stabilized solitons was further examined through soliton–soliton collision dynamics under different regimes, including the absence of self-steepening, uncompensated self-steepening, and the balanced self-steepening with $\mathcal{PT}$−symmetric gain–loss configuration. While collisions constitute strong perturbations that can enhance asymmetry and deformation, the balanced solitons were found to recover their structural integrity after interaction. This demonstrates that the stabilization mechanism identified in this work is robust rather than accidental and is not limited to ideal isolated propagation conditions.

The stability of the beam propagation analyzed in the perturbed system, and monitored the growth evolution. It provides a clear signature of the parameter regime in which stable $\mathcal{PT}$−symmetric soliton propagation is achieved.

The mapping of stability across system parameters $(s, W_0, \zeta, V_0, x_0, y_0)$ provides a quantitative guideline for designing non-Hermitian optical platforms capable of robust soliton transport. The methods and insights developed here pave the way for further exploration of $\mathcal{PT}$−controlled nonlinear localization, including higher-order solitons, vector beams with cross-phase modulation, and dynamically reconfigurable complex potentials.

Beyond fundamental interest, the proposed stabilization mechanism enables several concrete photonic functionalities. The suppression of self-steepening-induced beam walk-off provides a practical route toward drift-free soliton channels in planar and femtosecond-laser-written waveguides, where strong nonlinear gradients typically limit propagation fidelity. The parameter-selective balance between self-steepening and gain–loss further allows controlled nonlinear beam steering and routing by adjusting either the input intensity or the imaginary potential strength. Moreover, the coexistence of shape-preserving propagation with regulated power evolution suggests applications in spatial soliton amplifiers, where the beam profile remains intact while its energy is controlled through non-Hermitian coupling. In two-dimensional settings, the demonstrated control over transverse energy flow is particularly relevant for mode management in photonic lattices and highly nonlinear waveguides, where stable localization under strong nonlinear perturbations remains a longstanding challenge. Moreover, the stabilization mechanism discussed in this paper can

find applications in spatial mode selection and precision control of nonlinear energy channels, thereby extending applicability to advanced optical communication, nonlinear imaging, and photonic lattice engineering.

The present study opens several directions for future research. Extensions to higher-order nonlinear-gradient terms, nonlocal or saturable nonlinearities, and alternative classes of $\mathcal{PT}$–symmetric or non-Hermitian potentials may further enrich the understanding of transverse energy redistribution and stabilization mechanisms. Moreover, a systematic linear stability analysis, along with investigations of multi-soliton interactions and possible experimental realizations in engineered optical platforms, would be important steps toward assessing the robustness and applicability of the proposed framework.

CRediT authorship contribution statement

Jaseera C.P.: Writing – original draft, Software, Methodology, Investigation, Formal analysis, Data curation, Conceptualization. **Aysha Muhsina K.:** Writing – review & editing, Supervision, Investigation, Formal analysis, Data curation, Conceptualization.

Declaration of competing interest

The authors declare that they have no known competing financial interests or personal relationships that could have appeared to influence the work reported in this paper.

Data availability

All data supporting the findings of this study are included in this article.

References

[1] Agrawal G. Nonlinear fiber optics. In: Optics and photonics, Elsevier Science; 2013, URL https://books.google.co.in/books?id=xNvw-GDVn84C.
[2] Kivshar YS, Malomed BA. Dynamics of solitons in nearly integrable systems. Rev Modern Phys 1989;61:763–915. http://dx.doi.org/10.1103/RevModPhys.61.763, URL https://link.aps.org/doi/10.1103/RevModPhys.61.763.
[3] Segev M, Crosignani B, Yariv A, Fischer B. Spatial solitons in photorefractive media. Phys Rev Lett 1992;68:923–6. http://dx.doi.org/10.1103/PhysRevLett.68.923, URL https://link.aps.org/doi/10.1103/PhysRevLett.68.923.
[4] Efremidis NK, Sears S, Christodoulides DN, Fleischer JW, Segev M. Discrete solitons in photorefractive optically induced photonic lattices. Phys Rev E 2002;66:046602. http://dx.doi.org/10.1103/PhysRevE.66.046602, URL https://link.aps.org/doi/10.1103/PhysRevE.66.046602.
[5] Alberucci A, Piccardi A, Peccianti M, Kaczmarek M, Assanto G. Propagation of spatial optical solitons in a dielectric with adjustable nonlinearity. Phys Rev A 2010;82:023806. http://dx.doi.org/10.1103/PhysRevA.82.023806, URL https://link.aps.org/doi/10.1103/PhysRevA.82.023806.
[6] Swartzlander GA. Dark-soliton prototype devices: analysis by using direct-scattering theory. Opt Lett 1992;17(7):493–5, URL https://opg.optica.org/ol/abstract.cfm?URI=ol-17-7-493.
[7] Geng K, Mou D, Dai C. Nondegenerate solitons of 2-coupled mixed derivative nonlinear Schrödinger equations. Nonlinear Dynam 2023;(111):603–17. http://dx.doi.org/10.1007/s11071-022-07833-5.
[8] Mollenauer LF, Stolen RH, Gordon JP. Experimental observation of picosecond pulse narrowing and solitons in optical fibers. Phys Rev Lett 1980;45:1095–8. http://dx.doi.org/10.1103/PhysRevLett.45.1095, URL https://link.aps.org/doi/10.1103/PhysRevLett.45.1095.
[9] Jaseera CP, Aysha Muhsina K, Thasneem AR. Nonlinear light control in optical couplers: Harnessing PT-symmetry for enhanced beam propagation. Chaos: An Interdiscip J Nonlinear Sci 2025;35(2):023154. http://dx.doi.org/10.1063/5.0245649.
[10] Jaseera C, Muhsina KA. 2D PT-symmetric nonlinear couplers: Stability and power dynamics in sinusoidal system. Chaos: An Interdiscip J Nonlinear Sci 2025;35(8):083139. http://dx.doi.org/10.1063/5.0280866.
[11] Li L, Yu F. The fourth-order dispersion effect on the soliton waves and soliton stabilities for the cubic-quintic Gross–Pitaevskii equation. Chaos Solitons Fractals 2024;179:114377. http://dx.doi.org/10.1016/j.chaos.2023.114377, URL https://www.sciencedirect.com/science/article/pii/S0960077923012791.
[12] Biswas A, Milovic D. Optical solitons in a power law media with fourth order dispersion. Commun Nonlinear Sci Numer Simul 2009;14(5):1834–7. http://dx.doi.org/10.1016/j.cnsns.2008.08.008, URL https://www.sciencedirect.com/science/article/pii/S1007570408002682.
[13] Abdou B, Ndzana F, Tiofack C, Mohamadou A. Stability of one and two-dimensional spatial solitons in a cubic-quintic-septimal nonlinear Schrödinger equation with fourth-order diffraction and PT -symmetric potentials. Wave Motion 2021;107:102810. http://dx.doi.org/10.1016/j.wavemoti.2021.102810.
[14] Aysha Muhsina K, Subha PA. Stabilization of two-dimensional spatial solitons in dissipative media. Phys Scr 2014;89(7):075205. http://dx.doi.org/10.1088/0031-8949/89/7/075205.
[15] Aysha Muhsina K, Subha PA. Spatial solitons in a medium with lumped amplification and dissipation. J Nonlinear Opt Phys Mater 2015;24(01):1550011. http://dx.doi.org/10.1142/S0218863515500113.
[16] Tchepemen N, Tiofack C, Mohamadou A. Effect of power-law nonlinearity on PT -symmetric optical system with fourth-order diffraction. Commun Theor Phys (Beijing) 2020;72:9. http://dx.doi.org/10.1088/1572-9494/ab7ecf, URL https://iopscience.iop.org/article/10.1088/1572-9494/ab7ecf.
[17] Ostrovskaya EA, Kivshar YS, Skryabin DV, Firth WJ. Stability of multihump optical solitons. Phys Rev Lett 1999;83:296–9. http://dx.doi.org/10.1103/PhysRevLett.83.296, URL https://link.aps.org/doi/10.1103/PhysRevLett.83.296.
[18] Bo W-B, Wang R-R, Liu W, Wang Y-Y. Symmetry breaking of solitons in the PT-symmetric nonlinear Schrödinger equation with the cubic–quintic competing saturable nonlinearity. Chaos: An Interdiscip J Nonlinear Sci 2022;32(9):093104. http://dx.doi.org/10.1063/5.0091738.
[19] Bo WB, Wang RR, Fang Y, et al. Prediction and dynamical evolution of multipole soliton families in fractional Schrödinger equation with the PT-symmetric potential and saturable nonlinearity. Nonlinear Dynam 2023;111:1577–88. http://dx.doi.org/10.1007/s11071-022-07884-8.
[20] Bo W-B, Liu W, Wang Y-Y. Symmetric and antisymmetric solitons in the fractional nonlinear schrödinger equation with saturable nonlinearity and PT-symmetric potential: Stability and dynamics. Optik 2022;255:168697. http://dx.doi.org/10.1016/j.ijleo.2022.168697, URL https://www.sciencedirect.com/science/article/pii/S0030402622001097.
[21] Yan Z, Wen Z, Konotop VV. Solitons in a nonlinear Schrödinger equation with $\mathcal{PT}$-symmetric potentials and inhomogeneous nonlinearity: Stability and excitation of nonlinear modes. Phys Rev A 2015;92:023821. http://dx.doi.org/10.1103/PhysRevA.92.023821, URL https://link.aps.org/doi/10.1103/PhysRevA.92.023821.
[22] Lagrangian nonlocal nonlinear Schrödinger equations. Chaos Solitons Fractals 2022;156:111798. http://dx.doi.org/10.1016/j.chaos.2022.111798, URL https://www.sciencedirect.com/science/article/pii/S0960077922000091.

[23] Vinayagam P, Radha R, Al Khawaja U, Ling L. Collisional dynamics of solitons in the coupled PT symmetric nonlocal nonlinear Schrödinger equations. Commun Nonlinear Sci Numer Simul 2017;52:1–10. http://dx.doi.org/10.1016/j.cnsns.2017.04.011, URL https://www.sciencedirect.com/science/article/pii/S100757041730120X.

[24] Chen L, Wang Q, Shen M, Zhao H, Lin Y-Y, Jeng C-C, Lee R-K, Krolikowski W. Nonlocal dark solitons under competing cubic–quintic nonlinearities. Opt Lett 2013;38(1):13–5, URL https://opg.optica.org/ol/abstract.cfm?URI=ol-38-1-13.

[25] Wu H-Y, Jiang L-H, Wu Y-F. The stability of two-dimensional spatial solitons in cubic–quintic–septimal nonlinear media with different diffractions and PT -symmetric potentials. Nonlinear Dynam 2016;87. URL https://link.springer.com/article/10.1007/s11071-016-3141-2.

[26] dos Santos M, Bazeia D, Avelar A, et al. Spontaneous symmetry breaking induced by inhomogeneous nonlinearity in the coupled nonlinear Schrödinger equation. Nonlinear Dynam 2025;113:1539. http://dx.doi.org/10.1007/s11071-024-10274-x.

[27] Sudharsan J, Manikandan K, Aravinthan D. Stabilization of solitons in collisionally inhomogeneous higher-order nonlinear media with -symmetric harmonic-Gaussian potential with unbounded gain-loss distributions. Eur Phys J Plus 2022;137:860. http://dx.doi.org/10.1140/epjp/s13360-022-03081-z.

[28] He Y, Zhu X, Mihalache D, Liu J, Chen Z. Solitons in PT–symmetric optical lattices with spatially periodic modulation of nonlinearity. Opt Commun 2012;285(15):3320–4. http://dx.doi.org/10.1016/j.optcom.2012.04.006, URL https://www.sciencedirect.com/science/article/pii/S0030401812003537.

[29] Jaseera C, Aysha Muhsina K. Tunable wave propagation in nonlinear PT-symmetric systems: Stability and power switching of coupled symmetric and asymmetric modes. Chaos Solitons Fractals 2025;199:116873. http://dx.doi.org/10.1016/j.chaos.2025.116873, URL https://www.sciencedirect.com/science/article/pii/S0960077925008860.

[30] Han S-H, Park Q-H. Effect of self-steepening on optical solitons in a continuous wave background. Phys Rev E 2011;83:066601. http://dx.doi.org/10.1103/PhysRevE.83.066601, URL https://link.aps.org/doi/10.1103/PhysRevE.83.066601.

[31] Sheetal A, Sharma AK, Kaler R. Minimization of self-steepening of ultra short higher-order soliton pulse at 40Gb/s by the optimization of initial frequency chirp. Optik 2010;121(5):471–7. http://dx.doi.org/10.1016/j.ijleo.2008.08.009, URL https://www.sciencedirect.com/science/article/pii/S0030402608002246.

[32] Trippenbach M, Band YB. Effects of self-steepening and self-frequency shifting on short-pulse splitting in dispersive nonlinear media. Phys Rev A 1998;57:4791–803. http://dx.doi.org/10.1103/PhysRevA.57.4791, URL https://link.aps.org/doi/10.1103/PhysRevA.57.4791.

[33] DeMartini F, Townes CH, Gustafson TK, Kelley PL. Self-steepening of light pulses. Phys Rev 1967;164:312–23. http://dx.doi.org/10.1103/PhysRev.164.312, URL https://link.aps.org/doi/10.1103/PhysRev.164.312.

[34] Anderson D, Lisak M. Nonlinear asymmetric self-phase modulation and self-steepening of pulses in long optical waveguides. Phys Rev A 1983;27:1393–8. http://dx.doi.org/10.1103/PhysRevA.27.1393, URL https://link.aps.org/doi/10.1103/PhysRevA.27.1393.

[35] de Oliveira JR, de Moura MA, Hickmann JM, Gomes ASL. Self-steepening of optical pulses in dispersive media. J Opt Soc Am B 1992;9(11):2025–7, URL https://opg.optica.org/josab/abstract.cfm?URI=josab-9-11-2025.

[36] Moses J, Malomed BA, Wise FW. Self-steepening of ultrashort optical pulses without self-phase-modulation. Phys Rev A 2007;76:021802. http://dx.doi.org/10.1103/PhysRevA.76.021802, URL https://link.aps.org/doi/10.1103/PhysRevA.76.021802.

[37] Çelik EG, Antar N. Stabilization of self-steepening optical solitons in a periodic PT-symmetric potential. Chaos Solitons Fractals 2024;185:115125. http://dx.doi.org/10.1016/j.chaos.2024.115125, URL https://www.sciencedirect.com/science/article/pii/S0960077924006775.

[38] Jaseera CP, Aysha Muhsina K. Gradient-induced nonlinear beam transport and soliton asymmetry in PT-symmetric hyperbolic double-well optical potential. Eur Phys J Plus 2025;140:822. http://dx.doi.org/10.1140/epjp/s13360-025-06801-3.

[39] Signé EM, Djazet A, Megne LT, Djoko M, Fewo SI, Kofané TC. Control of self-steepening effects on dissipative light bullets via linear potential in a (3+1)D Ginzburg–Landau model. Nonlinear Dynam 2025;114(1):51. http://dx.doi.org/10.1007/s11071-025-11886-7, URL https://ui.adsabs.harvard.edu/abs/2025NonDy.114...51S.

[40] Çelik EG, Antar N. Bifurcation structure and stability of solitary waves in the cubic–quintic nonlinear Schrödinger equation with self-steepening. Eur Phys J Plus 2025;140:1104. http://dx.doi.org/10.1140/epjp/s13360-025-07053-x.

[41] Bender CM, Boettcher S. Real spectra in non-Hermitian Hamiltonians having $\mathcal{PT}$-symmetry. Phys Rev Lett 1998;80:5243–6, URL https://link.aps.org/doi/10.1103/PhysRevLett.80.5243.

[42] Bender CM, Brody DC, Jones, Hugh. Complex extension of quantum mechanics. Phys Rev Lett 2002;89:270401. http://dx.doi.org/10.1103/PhysRevLett.89.270401, URL https://link.aps.org/doi/10.1103/PhysRevLett.89.270401.

[43] Kottos T. Broken symmetry makes light work. Nat Phys 2010;6:166. http://dx.doi.org/10.1038/nphys1612.

[44] Guo A, Salamo GJ, Duchesne D, Morandotti R, Volatier-Ravat M, Aimez V, Siviloglou GA, Christodoulides DN. Observation of $\mathcal{PT}$–symmetry breaking in complex optical potentials. Phys Rev Lett 2009;103:093902, URL https://link.aps.org/doi/10.1103/PhysRevLett.103.093902.

[45] Ruter C, Makris K, El Ganainy R, et al. Observation of parity–time symmetry in optics. Nat Phys 2010;6. http://dx.doi.org/10.1038/nphys1515.

[46] Jaseera CP, Muhsina KA, Thasneem AR. Beam propagation in cubic-quintic nonlinear optical system supported by modified parity-time symmetric Rosen-Morse complex potential. Chaos: An Interdiscip J Nonlinear Sci 2024;34(7):073139. http://dx.doi.org/10.1063/5.0216963.

[47] Xu T-Z, Liu J-H, Dai C-Q, Wang X-Y. Multipole solitons of fractional second-third order nonlinear Schrödinger system with PT symmetric potential. Nonlinear Dynam 2025;113:32713–22. http://dx.doi.org/10.1007/s11071-025-11783-z.

[48] Mou D-S, Si Z-Z, Qiu W-X, Dai C-Q. Optical soliton formation and dynamic characteristics in photonic moiré lattices. Opt Laser Technol 2025;181:111774. http://dx.doi.org/10.1016/j.optlastec.2024.111774, URL https://www.sciencedirect.com/science/article/pii/S0030399224012325.

[49] Musslimani ZH, Makris KG, El-Ganainy R, Christodoulides DN. Optical solitons in $\mathcal{PT}-$ periodic potentials. Phys Rev Lett 2008;100:030402, URL https://link.aps.org/doi/10.1103/PhysRevLett.100.030402.

[50] Jaseera CP, Aysha Muhsina K. Beyond the symmetry: Exploring the nonlinear dynamics of 1D and 2D-symmetric sinusoidal systems. J Nonlinear Opt Phys Mater 2025;2550015. http://dx.doi.org/10.1142/S0218863525500158.

[51] Suneera TP, Subha PA. Parity-time symmetric coupler in transverse periodic and aperiodic potentials. Eur Phys J Plus 2018;133(10):1580–3. http://dx.doi.org/10.1140/epjp/i2018-11904-5.

[52] Thasneem AR, Subha PA, Aysha Muhsina K. Stationary states of parity-time symmetric dark solitons in super-Gaussian potential. Optik 2022;265:169518. http://dx.doi.org/10.1016/j.ijleo.2022.169518, URL https://www.sciencedirect.com/science/article/pii/S0030402622008294.

[53] Thasneem AR, Subha PA, Muhsina KA. The eigenstates of PT-symmetric coupled system with self-defocusing Kerr-nonlinearity. J Modern Opt 2024;71(1–3):63–74. http://dx.doi.org/10.1080/09500340.2024.2394971.

[54] Bendix O, Fleischmann R, Kottos T, Shapiro B. Exponentially fragile $\mathcal{PT}-$ symmetry in lattices with localized eigenmodes. Phys Rev Lett 2009;103:030402, URL https://link.aps.org/doi/10.1103/PhysRevLett.103.030402.

[55] Jaseera C, Muhsina KA, Thasneem A. Nonlinear eigen modes in optical media supported by cubic and quintic nonlinearities with parity-time symmetric hyperbolic complex potential. Optik 2024;311:171899. http://dx.doi.org/10.1016/j.ijleo.2024.171899, URL https://www.sciencedirect.com/science/article/pii/S0030402624002985.

[56] Jaseera CP, Muhsina KA, Thasneem AR. Stability of bright solitons in optical system supported by cubic and quintic nonlinearities with $\mathcal{PT}$-symmetric quartic harmonic complex potential. Phys Scr 2024;99(8):085266. http://dx.doi.org/10.1088/1402-4896/ad6537.

[57] Burlak G, Garcia-Paredes S, Malomed BA. PT-symmetric couplers with competing cubic-quintic nonlinearities. Chaos: An Interdiscip J Nonlinear Sci 2016;26(11):113103. http://dx.doi.org/10.1063/1.4966540.

[58] Dai CQ, Chen RP, Wang YY, Zhang YJ, Malomed BA. Dynamics of light bullets in inhomogeneous cubic–quintic–septimal nonlinear media with PT-symmetric potentials. Nonlinear Dynam 2017;87:1675–83. http://dx.doi.org/10.1007/s11071-016-3143-0.
[59] Zeng L, Malomed BA, Mihalache D, Zhu X. One- and two-dimensional solitons under the action of the inverted cubic–quintic nonlinearity. Commun Phys 2025;8(1):443. http://dx.doi.org/10.1038/s42005-025-02355-z.
[60] Jung PS, Pyrialakos GG, Pilka J, Kwasny M, Laudyn U, Trippenbach M, Christodoulides DN, Krolikowski W. Stable fundamental two-dimensional solitons in media with competing nonlocal interactions. Chaos Solitons Fractals 2023;171:113381. http://dx.doi.org/10.1016/j.chaos.2023.113381, URL https://www.sciencedirect.com/science/article/pii/S0960077923002825.
[61] Malomed BA. Multidimensional soliton systems. Adv Phys: X 2024;9(1):2301592. http://dx.doi.org/10.1080/23746149.2023.2301592.
[62] Fabrelli H, Sudharsan JB, Radha R, Gammal A, Malomed BA. Solitons under spatially localized cubic-quintic-septimal nonlinearities. J Opt 2017;19(7):075501. http://dx.doi.org/10.1088/2040-8986/aa7375.
[63] Kartashov YV, Malomed BA, Torner L. Solitons in nonlinear lattices. Rev Modern Phys 2011;83:247–305. http://dx.doi.org/10.1103/RevModPhys.83.247, URL https://link.aps.org/doi/10.1103/RevModPhys.83.247.
[64] Sastry SS. Introductory methods of numerical analysis. Prentice-Hall India; 2005, URL https://books.google.co.in/booksid=RhAOix1-wlYC.